Perpendicular magnetic anisotropy in ferrimagnetic Mn_4N films grown on $(LaAlO_3)_{0.3}(Sr_2TaAlO_6)_{0.7}$(001) substrates by molecular beam epitaxy

Taku Hirose[1], Taro Komori[1], Toshiki Gushi[1,2], Kaoru Toko[1], and Takashi Suemasu[1,a)]

[1]*Institute of Applied Physics, Graduate School of Pure and Applied Sciences, University of Tsukuba, Tsukuba, Ibaraki 305-8573, Japan*

[2]*Université Grenoble Alpes, CEA, CNRS, INAC-Spintec, 38000 Grenoble, France*

Many studies have shown that Mn_4N thin films possess perpendicular magnetic anisotropy (PMA) caused by in-plane tensile strain. Since cubic $(LaAlO_3)_{0.3}(Sr_2TaAlO_6)_{0.7}$ [LSAT] (001) has a smaller lattice constant than Mn_4N with a mismatch of 0.8%, a compressive strain is expected to be induced in Mn_4N epitaxial films grown on an LSAT substrate. We grew Mn_4N thin films on an LSAT(001) substrate by molecular beam epitaxy, and investigated the optimum growth temperature (T_S) from the aspects of crystallinity, magnetic properties, and magneto-transport properties. Mn_4N films were grown epitaxially at temperatures between T_S = 700 and 800 °C with maintaining PMA, and the optimum T_S was determined to be approximately 750 °C. In-plane and out-of-plane X-ray diffraction measurements showed that the Mn_4N films were under tensile stress in contrast to our prediction. From the thickness dependence of magnetization, a dead layer of approximately 10 nm existed at the Mn_4N/LSAT interface. Transmission electron microscopy observation revealed that Mn-N composites other than Mn_4N existed in the early stage of MBE growth.

[a)] Electronic mail: suemasu@bk.tsukuba.ac.jp

Keywords:

A1 Crystal structure

A3 Molecular beam epitaxy

B1 Mn_4N

B1 STO

B1 LSAT

B2 Magnetic materials

1. Introduction

Non-volatile memories using domain wall motion in ferrimagnetic nanowires driven with pulsed current, as has been proposed for racetrack memory and domain wall motion random access memory, have attracted increasing attention [1,2]. In such a domain wall motion device, a small spontaneous magnetization and perpendicular magnetic anisotropy (PMA) are required to increase the domain wall motion velocity and to reduce the threshold current for driving domain wall motion, respectively [3-5]. In addition to current-induced domain wall motion (CIDWM) by spin-transfer torque, CIDWM by spin–orbit torque (SOT) is also attracting attention, and it has been reported that PMA also has a high affinity with SOT [6-10]. We focus on Mn_4N thin films as a material suitable for CIDWM. Mn_4N has an anti-perovskite structure as shown in Fig. 1. Here, we define the corner and face-centered atomic sites as I and II, respectively. The II sites are further divided into IIA and IIB sites in the presence of magnetization (arrow in Fig. 1). Mn_4N has been reported to have a small spontaneous magnetization of 10^2 kA/m and PMA with a magnetic anisotropy constant K_u of 10^2 kJ/m^3 [11]. In addition, it is a rare-earth free material and consists of only inexpensive elements. Especially, in Mn_4N thin films formed on $SrTiO_3$[STO](001) substrates, which have a small lattice mismatch to Mn_4N of approximately –0.4%, it was reported that magnetic domains with a millimeter size appeared [12]. Furthermore, a domain wall motion velocity of approximately 900 m/s was achieved for Mn_4N wires on STO(001) [13]. Recently, it has been suggested that partial substitution of Mn atoms with Ni atoms causes magnetic compensation at room temperature (RT) [14,15], which leads to the existence of an angular momentum compensation point at which the domain wall motion velocity can be dramatically increased. Although the origin of PMA has yet to be clarified, we

consider it to arise from in-plane tensile strain in Mn_4N thin films [16]. Bulk Mn_4N has an easy axis in the [111] direction [17]. In contrast, Mn_4N thin films fabricated on glass [18], Si(001)[19,20], 6H-SiC(001) [21], MgO(001) [16,22-25], and STO(001) [16,26,27] showed PMA along the *c*-axis orientation. MgO(001) and STO(001) substrates have larger lattice constants than Mn_4N and the lattice mismatch is approximately −7.6% and −0.4%, respectively, and the presence of in-plane tensile strain was confirmed by X-ray diffraction measurement for such Mn_4N thin films. On the other hand, an $(LaAlO_3)_{0.3}(Sr_2TaAlO_6)_{0.7}$[LSAT](001) substrate has a smaller lattice constant than Mn_4N with a lattice mismatch of +0.8%. Therefore, compressive strain is expected to be introduced into Mn_4N epitaxial thin films on LSAT(001) substrates. However, there have been no reports on the growth of Mn_4N thin films on such substrates, which may result in a compressive strain in Mn_4N films.

In this paper, we grew Mn_4N thin films by molecular beam epitaxy (MBE) on LSAT(001) substrates and varied the substrate growth temperature (T_S) to form epitaxial films. T_S was compared with those on STO(001) substrates. Furthermore, we investigated how the magnetic and the magneto-transport properties of Mn_4N films changed depending on the film thickness. As a result, we succeeded in achieving epitaxial growth of Mn_4N thin films on LSAT(001) at T_S = 700−800 °C with PMA. We also confirmed that the in-plane tensile strain was present even in Mn_4N epitaxial films on LSAT(001).

2. Materials and Methods

2-1 Preparation of Mn_4N films on LSAT(001) and STO(001)

We grew approximately 10−30 nm-thick Mn_4N thin films on STO(001) and on

LSAT(001) single crystal substrates using an MBE chamber equipped with a standard Knudsen cell (K-cell) of Mn and a radio frequency nitrogen plasma. T_S was varied in the range 350–550 °C for Mn_4N films grown on STO(001). However, T_S was set at 450–800 °C for Mn_4N films on LSAT(001). Prior to thin-film growth, we washed the STO(001) substrates with organic solvent (acetone, methanol each for 2 min.), deionized water for 2 min., and etched with buffered hydrofluoric acid for 30 s. As for the treatment of LSAT substrates, we cleaned them with only organic solvent (acetone and methanol each for 5 min.). The nitrogen plasma power was set at 107–112 W with a nitrogen flow rate of 0.9–1.0 sccm so that the pressure during the growth was approximately 4×10^{-5} Torr in the chamber. The deposition rate of Mn was controlled to be 1.0–1.1 nm/min by setting the crucible temperature of the Mn K-cell at 835 °C. In addition, Ta or Ti was sputtered in situ onto Mn_4N films as a capping layer to prevent oxidation. Furthermore, we also grew 10–40-nm-thick Mn_4N films on LSAT(001) at T_S = 750 °C. The sample preparation details are summarized in Table 1. The crystalline quality of the grown films was characterized by reflection high-energy electron diffraction (RHEED), and out-of-plane and in-plane X-ray diffraction (XRD) measurements with a Cu-Kα radiation source. Ge(220) single crystals were used to make the X-rays monochromatic. The film thickness was evaluated by X-ray reflectivity. Cross sectional transmission electron microcopy (X-TEM) observations were performed using FEI Tecnai Osiris operated at 200 kV, equipped with an energy dispersive X-ray spectrometer (EDX). The X-TEM sample was prepared by the conventional focused ion beam method. The surface roughness was measured by an atomic force microscope.

2-2 Evaluation of magnetic properties and surface properties of Mn_4N films

The magnetization and magnetic field loops (*M-H* loops) were measured at RT by a vibrating sample magnetometer. Moreover, regarding the uniaxial magnetic anisotropy constant K_u, the effective magnetic anisotropy constant K_u^{eff} was calculated from the data equivalent to the magnetization versus magnetic field (*M-H*) loop by the anomalous Hall effect (AHE) measurement, because the Hall voltage is proportional to $M_\perp/M_S$. Here, $M_\perp$ and M_S are the vertical component of the magnetization and the spontaneous magnetization, respectively. The uniaxial anisotropy constant was acquired by adding the demagnetizing field component $2\pi M_S^2$ to the anisotropy constant K_u^{eff} obtained by the experiment as,

$$K_u = K_u^{eff} + \frac{1}{2}\mu_0 M_S^2, \tag{1}$$

$$K_u^{eff} = \left(\mu_0 \int_0^{M_S} H dm\right)_{hard} - \left(\mu_0 \int_0^{M_S} H dm\right)_{easy}. \tag{2}$$

Here, easy (hard) indicates the magnetization easy axis (hard axis). Assuming that the shape of the thin film is square,

$$M_{||} = M_S \sqrt{1 - \left(\frac{M_\perp}{M_S}\right)^2}. \tag{3}$$

Here, $M_{||}$ is the in-plane component of magnetization [11]. A physical property measurement system (PPMS, Quantum Design) was used to measure the anomalous Hall effect.

3. Results

Regarding the results of thin-film growth, we mainly focus on those obtained for LSAT(001) substrates because the epitaxial growth of Mn_4N films on STO(001) was already reported on the basis of streaky RHEED patterns and *c*-axis-oriented XRD

profiles [11,12,16,25]. Fig. 2(a) and 2(b) show RHEED patterns of STO(001) and LSAT(001) substrates, respectively, observed along the [100] azimuth just before the growth of Mn_4N films. Fig. 2(c)–(h) shows RHEED patterns observed along the LSAT[100] azimuth for Mn_4N films on LSAT(001) substrates at T_S = 450, 550, 650, 700, 750, and 800 °C (MNLSAT1–6), respectively. The RHEED images present sharp streak lines for samples grown at T_S = 700, 750, and 800 °C. However, for samples grown at lower T_S (< 700 °C), ring patterns were observed in the RHEED images.

Fig. 3(a) shows the out-of-plane XRD profiles for grown films on an LSAT substrate at T_S = 450–800 °C. Here, the diffraction peaks of the Mn_4N films overlapped with those of LSAT, showing that the out-of-plane lattice constant of Mn_4N films (c) was close to that of LSAT. Together with the streaky RHEED patterns in Fig. 2, it was concluded that c-axis-oriented Mn_4N films were epitaxially grown at T_S = 700–800 °C. Fig. 3(b) shows the in-plane XRD profiles. We observed the presence of the Mn_4N 400 diffraction peaks marked by arrows for samples grown at T_S = 700, 750, and 800 °C at $2\theta_\chi$ angles a little smaller than those of the LSAT 400 diffraction peaks, meaning that the Mn_4N films have a larger in-plane lattice constant (a) than the LSAT. To make the diffraction angles clear, we take MNLSAT5, Mn_4N films grown at T_S=750 °C, for example. Figure 4 shows the enlarged XRD profiles at around 2θ, $2\theta_\chi$ = 106° for this sample. We see in the out-of-plane XRD profiles that the Mn_4N 004 diffraction peak denoted by the triangle appeared at 2θ angles a little higher than the LSAT 004 diffraction peak, meaning that the c of Mn_4N films was smaller than that of LSAT. In contrast, the Mn_4N 400 diffraction peak in the in-plane XRD profile appeared at a slightly smaller angle $2\theta_\chi$ than the LSAT 400 diffraction peak, indicating that the a of Mn_4N films was larger than that of the LSAT. These results revealed that the Mn_4N film

on the LSAT (001) substrate was subjected to in-plane tensile strain ($c/a < 1$) differently from the prediction. The same result was confirmed for other samples grown at T_S=700 and 800 °C. According to the first-principle calculations [26], Mn_4N with c/a = 0.98 is predicted to be a more stable phase than that with c/a = 1 from the viewpoint of formation energy. We thus speculate that the introduction of compressive stress into Mn_4N films in the in-plane direction is difficult. Regarding the nitrogen supply during the growth, it was controlled by the pressure in the growth chamber as the beam flux monitor was not attached to the growth chamber. Fig. 5(a)–(c) show examples of how the nitrogen supply affected the RHEED patterns of Mn_4N films, observed for 30-nm-thick Mn_4N films grown at T_S = 750 °C with different pressures varied as 3.8×10^{-5}, 3.9×10^{-5}, and 4.0×10^{-5} Torr, respectively. Based on these results, we chose the pressure to be 3.9×10^{-5} Torr for Mn_4N films at T_S = 750 °C. For Mn_4N films grown at T_S = 700 and 800 °C, possessing streaky RHEED patters (MNLSAT4 and 6), the nitrogen supply was optimized in the same way.

Fig. 6 shows the *M-H* loops of normalized magnetization (M/M_S) for samples MNLSAT4–6 measured using AHE by PPMS. The red line and blue broken line indicate normalized magnetization when H // [100] and H // [001], respectively, which showed that they possessed PMA at RT.

We next compared the T_S dependences of M_S and K_u for Mn_4N films grown on LSAT(001) with those on STO(001) as shown in Fig. 7(a) and 7(b), respectively. The values of K_u were obtained only for samples grown at T_S = 700–800 °C because the other samples did not show hysteresis loops in the *M-H* curves owing to their poor magnetizations. It was found that M_S increased with the increase of T_S and reached a maximum at T_S = 700 and 750 °C, as shown in Fig. 7(a). This was presumably because

the degree of *c*-axis orientation of Mn_4N films increased with T_S. However, at T_S = 800 °C, the M_S decreased. This was because this temperature of 800 °C was close to 860 °C above which Mn_4N becomes unstable according to the phase diagram [28]. On the basis of these results, we concluded that the optimum T_S of Mn_4N films on LSAT(001) was 750 °C. We next determined the optimum T_S for Mn_4N films on STO(001). The detailed growth condition of Mn_4N films on STO(001) has been reported previously [16]. Fig. 7(b) shows the T_S dependences of M_S and K_u for Mn_4N films grown on STO(001) substrates. The values of M_S and K_u remained almost unchanged for samples grown at T_S = 400–500 °C except for the sample at T_S = 350 °C (MNSTO1). When grown at $T_S \geq 400$ °C (MNSTO2–5), Mn_4N thin films with PMA and good magnetic properties were obtained. Table 2 summarizes the root-mean-square (RMS) surface roughness values of the Mn_4N films grown on STO(001) and LSAT(001) substrates for various T_S. Regarding the Mn_4N thin films on STO(001), the RMS roughness values of MNSTO3, grown at T_S = 450 °C, reached a minimum of 0.32 nm. As T_S increased, the surface roughness RMS value increased. Therefore, it can safely be stated that the optimum T_S was approximately 450 °C in this case.

We next investigated the thickness (*d*) dependence of the magnetization of Mn_4N thin films on LSAT(001) substrates at T_S = 750 °C. The film thickness *d* was varied from 10 to 39 nm. Fig. 8(a)-(e) shows the film thickness dependence of RHEED patterns of samples on LSAT(001) substrates grown at T_S = 750 °C observed along the LSAT[100] azimuth. Regarding MNLSAT7 (*d* = 10 nm), the RHEED image exhibited a mixture of rings and spots. For this sample, phases other than Mn_4N were formed, as shown later. With increasing *d* from 10 to 20 nm, a sharp streaky RHEED pattern with Kikuchi lines appeared in the sample MNLSAT8. At *d* = 30 and 40 nm, similar streaky

RHEED patterns were obtained. Fig. 8(f) shows the out-of-plane XRD profiles of these samples. These results suggested that we succeeded in growing highly *c*-axis oriented Mn_4N thin epitaxial films on LSAT substrates in the range d = 20–40 nm.

Fig. 9(a) shows the raw *M-H* loops of samples with d = 10–40 nm with the external magnetic field applied perpendicular to the plane normalized by sample area. We observed that the *M-H* loop changed continuously with respect to d in the range d = 20–40 nm. PMA was distinctly evident for these samples. However, the hysteresis loop was missing for the sample MNLSAT7 at d = 10 nm. Fig. 9(b) shows the d dependence of the spontaneous magnetization of Mn_4N films grown on an LSAT substrate. The measured values showed the magnetizations per unit area. The contribution of the LSAT substrate to the measured magnetization was subtracted. The linear extrapolation intersected the *x*-axis at approximately d = 11 nm. This result indicated the presence of a dead layer of approximately 10 nm in the film grown on LSAT substrates. Similar dead layers have been reported in CoFeB thin films [29]. However, such dead layers were not observed for Mn_4N/STO(001) interface [13]. We attributed this dead layer to denitrification during substrate heating [30].

To see what happens when the layer thickness is small, we performed X-TEM observations on sample MNLSAT7 (d = 10 nm). Sample MNLSAT8 (d = 20 nm) was used for comparison. Fig. 10(a) and 10(b) show the X-TEM and EDX images of Mn and La, respectively, for sample at d = 10 nm. The grown film was found to be composed of small grains. In Fig. 10(b), the averaged atomic ratio of Mn to N in the green-colored region of grain A is approximately 9, differently from that in Mn_4N. On the other hand, in grain B, the ratio is close to 4, meaning that grain B is Mn_4N. Other ratios such as approximately 7 were observed in other regions. These results indicate

that Mn-N composites other than Mn_4N are formed. Considering that the *M-H* loop of MNLSAT7 (d = 10 nm) is not open in Fig. 9(a), the volume ratio of ferrimagnetic Mn_4N grains to the other non-magnetic grains is supposed to be small. Fig. 10(c) shows the X-TEM for sample at d = 20 nm. In contrast to Fig. 10(a), the grown film is flat. Fig. 10(d) is its magnified view, wherein we can see lattices of Mn_4N. From these results, we can at least state that Mn-N composites other than Mn_4N, observed at d = 10 nm in Fig. 10(b), converted into Mn_4N when d increased from 10 nm to 20 nm.

4. Conclusions

We succeeded in growing *c*-axis oriented epitaxial Mn_4N thin films on LSAT(001) substrates with PMA, at T_S = 700–800 ℃ by MBE. It was also found that Mn_4N epitaxial thin films showed in-plane tensile strain even though an LSAT(001) substrate would induce in-plane compressive distortion to Mn_4N from the viewpoint of the lattice mismatch between the two materials. Because the K_u became a maximum and the RMS surface roughness values reached a minimum at T_S =750 °C, we conclude that 750 °C is the most adequate T_S to grow Mn_4N films on an LSAT(001) substrate by MBE. From the d dependence of magnetization, a dead layer of approximately 10 nm in thickness existed at the Mn_4N/LSAT interface for Mn_4N films at T_S = 750 °C. TEM observation revealed that Mn-N composites other than Mn_4N existed in the early stage of MBE growth.

Acknowledgements

TEM samples were prepared at the Nanotechnology Platform of the University of Tsukuba by Ms. T. Tawara and Mr. S. Tanigawa using FIB-SEM. TEM observation was

performed by Dr. N. Yoshizawa and Mr. N. Saitoh of AIST, Japan. The authors acknowledge Dr. L. Vila and Dr. J. P. Attanè of Universitè Grenoble Aples, CNRS, CES, for fruitful discussion and encouragement to pursue this work. The authors also acknowledge Dr. S. Fusil and Dr. M. Bibes, CNRS Thales, for LSAT(001) substrates. Magnetization measurements were performed with the help of Professor H. Yanagihara of the University of Tsukuba, and Associate Professor T. Koyano of Cryogenics Division of the University of Tsukuba. This work was financially supported by the Ministry of Education, Culture, Sports, Science and Technology of Japan (KAKENHI Nos. 19K04499, 19K21954, and 19KK0104).

Table 1 Layer structure of samples MNLSAT1–10 on LSAT(001). Substrate temperature (T_S), Mn_4N film thickness (t_{Mn4N}), and film thickness of cap layer (t_{cap}) are specified.

Sample	T_S [°C]	t_{Mn4N} [nm]	t_{cap} [nm]
MNLSAT1	450	16.5	3.0
MNLSAT2	550	23.9	3.5
MNLSAT3	650	23.3	3.1
MNLSAT4	700	33.1	2.1
MNLSAT5	750	31.0	1.3
MNLSAT6	800	30.6	4.1
MNLSAT7	750	10.0	3.9
MNLSAT8	750	19.7	3.2
MNLSAT9	750	38.7	4.1

Table 2 T_S dependence of surface roughness RMS values of Mn_4N films (MNLSAT1−6) on LSAT(001) and those (MNSTO1−5) on STO(001).

Sample	T_S [°C]	RMS [nm]	Sample	T_S [°C]	RMS [nm]
MNLSAT1	450	0.45	MNSTO1	350	1.20
MNLSAT2	550	0.40	MNSTO2	400	0.54
MNLSAT3	650	1.60	MNSTO3	450	0.32
MNLSAT4	700	1.44	MNSTO4	500	1.04
MNLSAT5	750	2.07	MNSTO5	550	4.04
MNLSAT6	800	6.17			

Figure captions

Figure 1 Schematic illustration of the crystal structure of Mn_4N. Mn_4N has an anti-perovskite structure. Mn atoms are positioned at corner (I-site) and face-centered sites (II-site). II sites can be further divided into IIA and IIB sites with magnetization (arrow). N atom is located at the body center.

Figure 2 RHEED patterns of (a) STO(001) and (b) LSAT(001) substrates observed along its [100] azimuth just before the growth of Mn_4N films. (c)-(h) RHEED patterns of grown films on LSAT(001) substrates at T_S = 450, 550, 650, 700, 750, and 800 °C (MNLSAT1–6), respectively, along the LSAT[100] azimuth.

Figure 3 (a) Out-of-plane and (b) in-plane XRD patterns of samples on LSAT (001) substrates at T_S = 450, 550, 650, 700, 750, and 800 °C (MNLSAT1–6). Arrows indicate the peak position of Mn_4N 400 reflection.

Figure 4 Enlarged out-of-plane and in-plane XRD profiles at around 2θ, $2\theta_\chi = 106°$ for the LSAT substrate and MNLSAT5, Mn_4N films grown at T_S=750 °C.

Figure 5 RHEED patterns of 30-nm-thick Mn_4N films on LSAT(001) substrates at T_S = 750 °C along the LSAT[100] azimuth. Pressures during the growth are (a) 3.8×10^{-5}, (b) 3.9×10^{-5}, and (c) 4.0×10^{-5} Torr.

Figure 6 Normalized *M*-*H* loops (M/M_S) for MNLSAT4–6 measured using AHE by PPMS. Red line and blue broken line indicate normalized magnetization when *H* //

[100], and H // [001], respectively.

Figure 7 Growth temperature dependence of spontaneous magnetization (M_S) and uniaxial magnetic anisotropy constant (K_u) of Mn_4N films on (a) LSAT(001) and (b) STO(001) substrates.

Figure 8 Film thickness dependence of RHEED patterns of samples observed along the LSAT[100] azimuth with d = (a) 0, (b) 10, (c) 20, (d) 31, and (e) 39 nm on LSAT(001) substrates grown at 750 °C. (g) Out-of-plane XRD profiles of these samples.

Figure 9 (a) Raw M-H loops of samples with d = 10–39 nm with the external magnetic field applied perpendicular to the plane. (b) Grown layer thickness dependence of spontaneous magnetization (M_S) of Mn_4N films grown on an LSAT substrate. The measured values show magnetizations per unit area.

Figure 10 (a) X-TEM and (b) EDX images of Mn and La of MNLSAT7 (d = 10 nm). (c) X-TEM image of MNLSAT8 (d = 20 nm) and (d) magnified view of (c). Ti is used as a capping layer.

[1] S. S. P. Parkin, M. Hayashi, L. Thomas, Science 320 (2008) 190.
[2] S. Fukami, T. Suzuki, K. Nagahara, N. Ohshima, Y. Ozaki, S. Saito, R. Nebashi, N. Sakimura, H. Honjo, K. Mori, C. Igarashi, S. Miura, N. Ishiwata, T. Sugibayashi, 2009 Symposium on VLSI Technology, Digest Tech. Pap., 2009, p. 230.
[3] I. M. Miron, T. Moore, H. Szambolics, L.D. Buda-Prejbeanu, S. Auffret, B. Rodmacq, S. Pizzini, J. Vogel, M. Bonfim, A. Schuhl, G. Gaudin, Nat. Mater. 10 (2011) 419.
[4] A. J. Schellekens, A. van den Brink, J. H. Franken, J. J. M. Swagten, B. Koopmans, Nat. Commun. 3 (2012) 847.
[5] A. Thiaville, Y. Nakatani, J. Miltat, N. Vernier, J. Appl. Phys. 95 (2004) 7049.
[6] H. Kurebayshi, J. Sinova, D. Fang, A.C. Irvine, T.D. Skinner, J. Wunderlich, V. Novak, R. P. Campion, B. L. Gallagher, E. K. Vehstedt, L. P. Zarbo, K. Vyborny, A. J. Ferguson, T. Jungwirth, Nat. Nanotech. 9 (2014) 211.
[7] I. M. Miron, G. Gaudin, S. Auffret, B. Rodmacq, A. Schuhl, S. Pizzini, J. Vogel, P. Gambardella, Nat. Mater. 9 (2010) 230.
[8] E. Martinez, S. Emori, G. S. D. Beach, Appl. Phys. Lett. 103 (2013) 072406.
[9] S. H. Yang, K.S. Ryu, S. Parkin, Nat. Nanotech. 10 (2015) 221.
[10] D. Bang, H. Awano, Appl. Phys. Express 5 (2012) 12.
[11] T. Komori, A. Anzai, T. Gushi, K. Toko, T. Suemasu, J. Cryst. Growth. 507 (2019) 163.
[12] T. Gushi, L. Vila, O. Fruchart, A. Marty, S. Pizzini, J. Vogel, F. Takata, A. Anzai, K. Toko, T. Suemasu, Jpn. J. Appl. Phys. 57 (2018) 12.
[13] T. Gushi, M. J. Klug, J. Pena Garcia, G. Sambit, J.P. Attane, H. Okuno, O. Fruchart, J. Vogel, T. Suemasu, S. Pizzini, and L. Vila, NANO Letters 19 (2019) 8716.
[14] T. Komori, T. Gushi, A. Anzai, L. Vila, J. P. Attene, S. Pizzini, J. Vogel, S. Isogami, K. Toko, T. Suemasu, J. Appl. Phys. 125 (2019) 213902.
[15] T. Komori, T. Hirose, T. Gushi, K. Toko, T. Hanashima, J. P. Attane, L. Vila, K. Amemiya, and T. Suemasu, J. Appl. Phys. 127 (2020) 043903.
[16] Y. Yasutomi, K. Ito, T. Sanai, K. Toko, T. Suemasu, J. Appl. Phys. 115 (2014) 17A935.
[17] C. D. Stanciu, A. V. Kimel, F. Hansteen, A. Tsukamoto, A. Itoh, A. Kirilyuk, Phys.

Rev. B73 (2006) 220402.
[18] K.M. Ching, W.D. Chang, T.S. Chin, J. Alloys Compd. 222 (1995) 184.
[19] D. Fruchart, D. Givord, P. Convert, P. l'Heritier, J.P. Senateur, J. Phys. F: Metal Phys., 9 (1979) 12.
[20] K. M. Ching, W.D. chang, T.S. Chin, Appl. Surf. Sci., 92 (1996) 471.
[21] D. Dhar, O. Brandt, H. Ploog, Appl. Phys. Lett. 86 (2005) 112504.
[22] X. Shen, A. Chikamatsu, K. Shigematsu, Y. Hirose, T. Fukumura, T. Hasegawa, Appl. Phys. Lett. 105 (2014) 072410.
[23] M. Meng, S.X. Wu, L.Z. Ren, W.Q. Zhou, Y.J. Wang, G.L. Wang, S.W. Li, Appl. Phys. Lett. 106 (2015) 032407.
[24] K. Kabara, M. Tsunoda, J. Appl. Phys. 117 (2015) 17B512.
[25] A. Anzai, F. Takata, T. Gushi, K. Toko, T. Suemasu, J. Cryst. Growth 489 (2018) 20.
[26] K. Ito, Y. Yasutomi, K. Kabara, T. Gushi, S. Higashikozono, K. Toko, M. Tsunoda, and T. Suemasu, AIP Adv. 6, 056201 (2016).
[27] A. Foley, J. Corbett, A. Khan, A.L. Richard, D.C. Ingram, A.R. Smith, L. Zhao, J. C. Gallagher, F. Yang, J. Magn. Magn. 439 (2017) 236.
[28] Journal of phase equilibria vol.15 no.4 p451 (1994).
[29] Y. H. Wang, W.C. Chen, S.Y. Yang, K.H. Shen, J. Appl. Phys. 99 (2006) 08M307.
[30] M. Meng, S. Li, M. Saghayezhian, E.W. Plummer, R. Jin, Appl. Phys. Lett. 112 (2018) 132402.

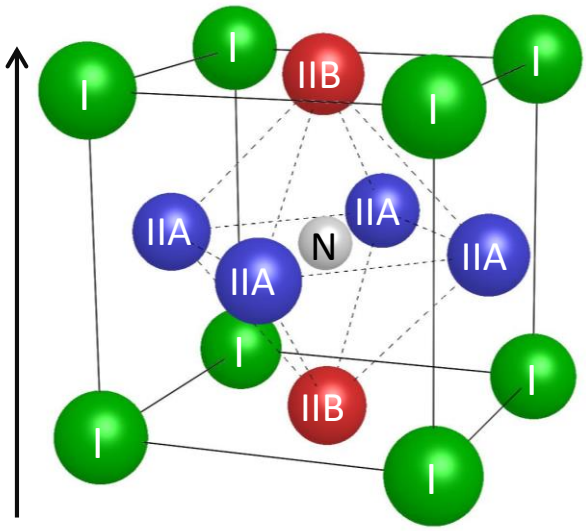

Fig. 1

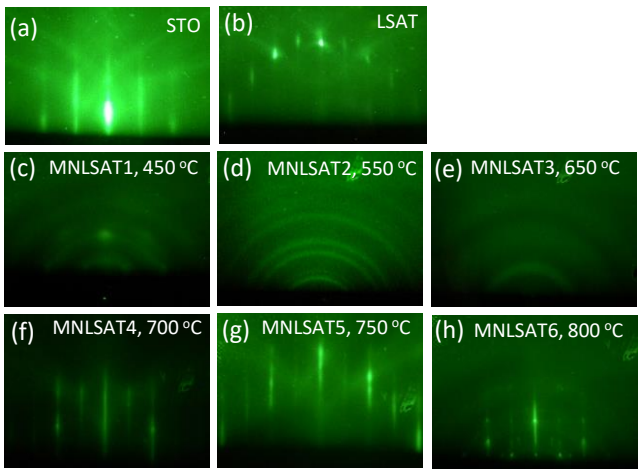
(a) STO
(b) LSAT
(c) MNLSAT1, 450 °C
(d) MNLSAT2, 550 °C
(e) MNLSAT3, 650 °C
(f) MNLSAT4, 700 °C
(g) MNLSAT5, 750 °C
(h) MNLSAT6, 800 °C

Fig. 2

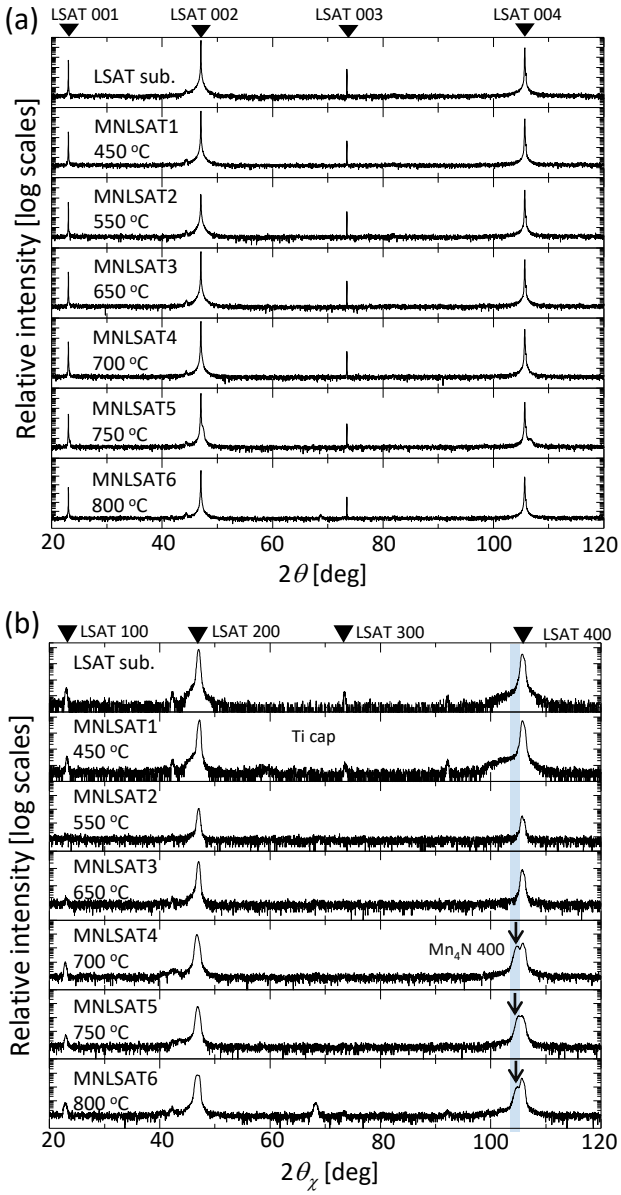
(a)
LSAT 001
LSAT 002
LSAT 003
LSAT 004
LSAT sub.
MNLSAT1
450 °C
MNLSAT2
550 °C
MNLSAT3
650 °C
MNLSAT4
700 °C
MNLSAT5
750 °C
MNLSAT6
800 °C
Relative intensity [log scales]
20
40
60
80
100
120
2θ [deg]
(b)
LSAT 100
LSAT 200
LSAT 300
LSAT 400
LSAT sub.
MNLSAT1
450 °C
Ti cap
MNLSAT2
550 °C
MNLSAT3
650 °C
MNLSAT4
700 °C
Mn4N 400
MNLSAT5
750 °C
MNLSAT6
800 °C
Relative intensity [log scales]
20
40
60
80
100
120
2θχ [deg]

Fig. 3

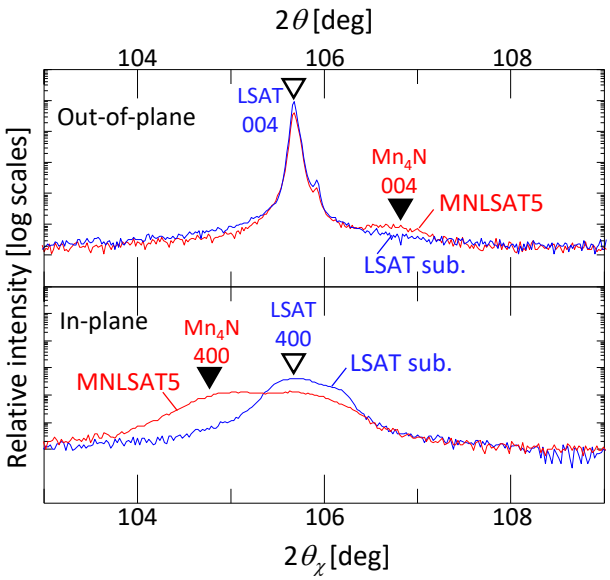
2θ [deg]
104
106
108
Out-of-plane
LSAT
004
Mn4N
004
MNLSAT5
LSAT sub.
In-plane
Mn4N
400
LSAT
400
MNLSAT5
LSAT sub.
Relative intensity [log scales]
104
106
108
2θχ [deg]

Fig. 4

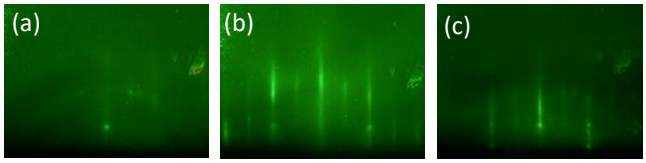

Fig. 5

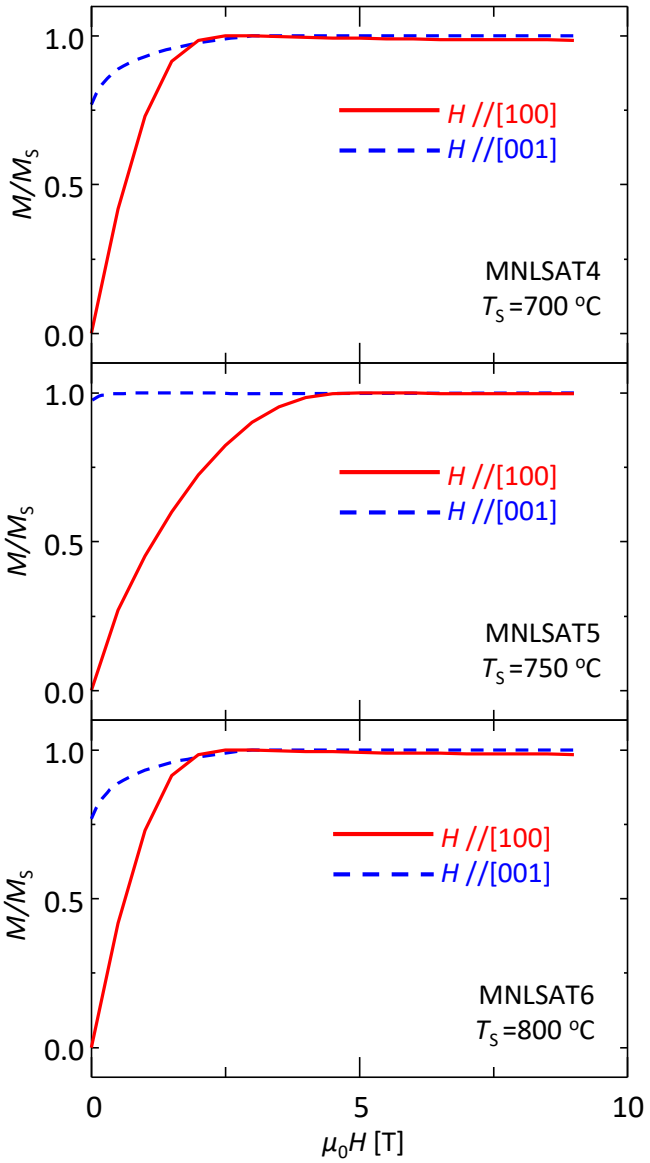
1.0
0.5
0.0
M/M_S
H //[100]
H //[001]
MNLSAT4
T_S =700 °C
MNLSAT5
T_S =750 °C
MNLSAT6
T_S =800 °C
0
5
10
μ_0H [T]

Fig. 6

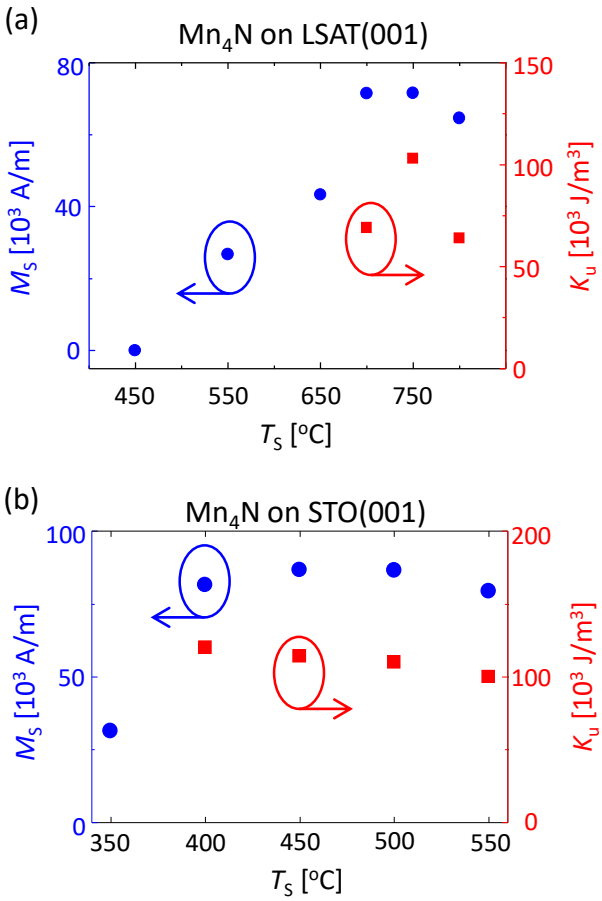
(a)
Mn4N on LSAT(001)
80
40
0
150
100
50
0
450
550
650
750
Ts [°C]
Ms [10³ A/m]
Ku [10³ J/m³]
(b)
Mn4N on STO(001)
100
50
0
200
100
0
350
400
450
500
550
Ts [°C]
Ms [10³ A/m]
Ku [10³ J/m³]

Fig. 7

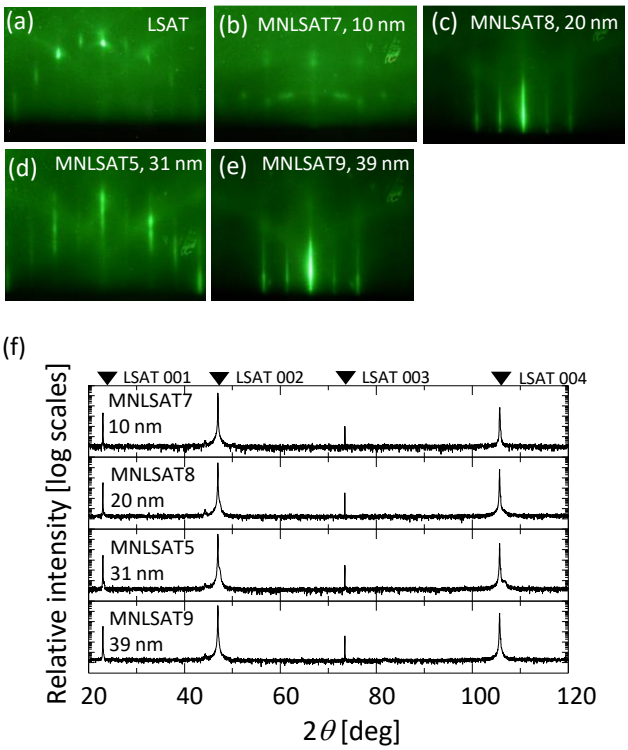
(a) LSAT
(b) MNLSAT7, 10 nm
(c) MNLSAT8, 20 nm
(d) MNLSAT5, 31 nm
(e) MNLSAT9, 39 nm
(f)
LSAT 001
LSAT 002
LSAT 003
LSAT 004
MNLSAT7
10 nm
MNLSAT8
20 nm
MNLSAT5
31 nm
MNLSAT9
39 nm
Relative intensity [log scales]
20
40
60
80
100
120
2θ [deg]

Fig. 8

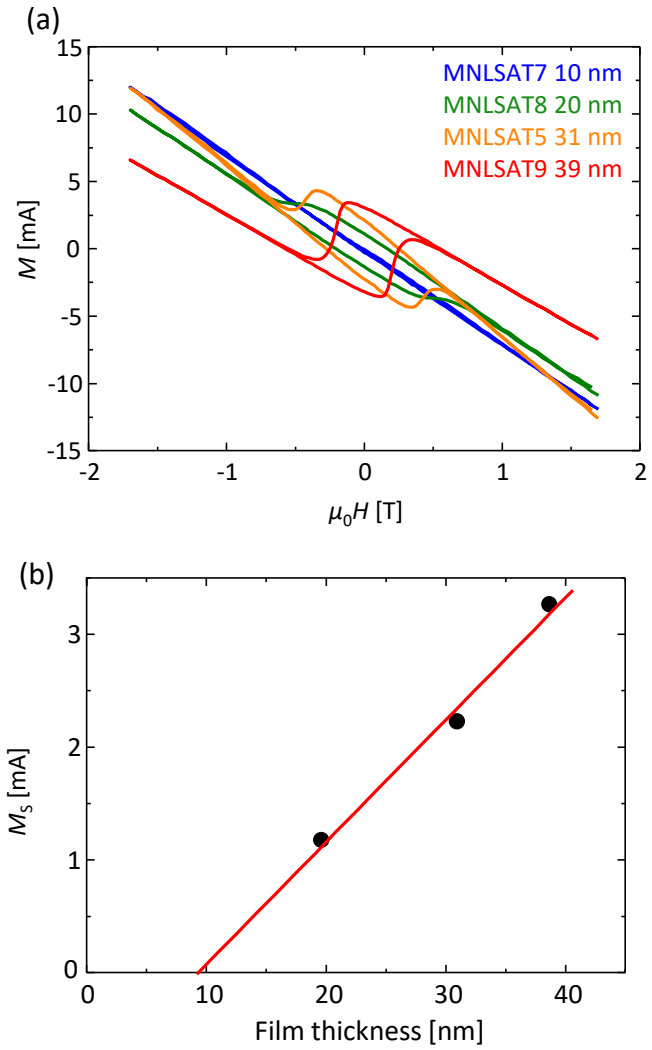
(a)
MNLSAT7 10 nm
MNLSAT8 20 nm
MNLSAT5 31 nm
MNLSAT9 39 nm
M [mA]
μ0H [T]
(b)
MS [mA]
Film thickness [nm]

Fig. 9

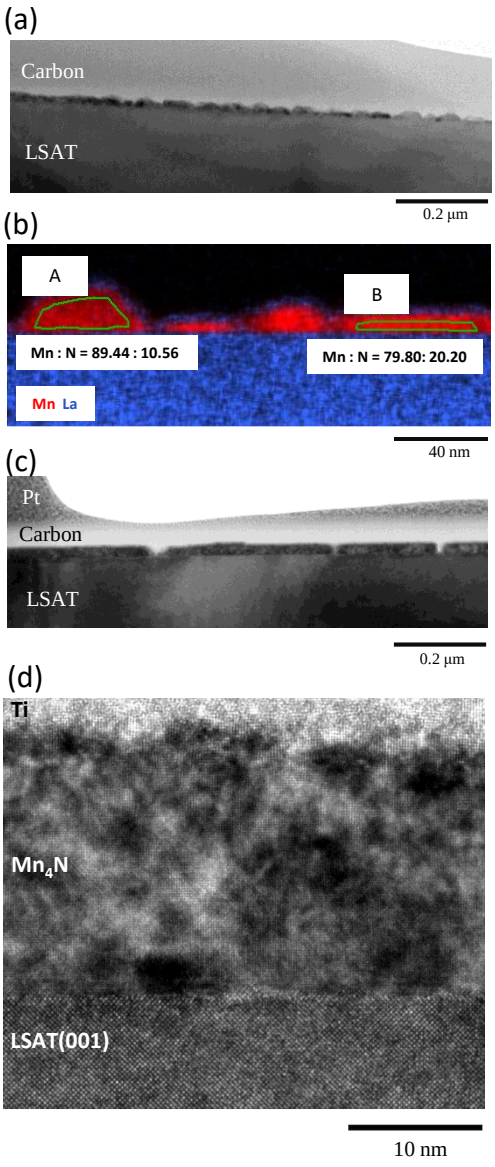
(a)
Carbon
LSAT
0.2 µm
(b)
A
B
Mn : N = 89.44 : 10.56
Mn : N = 79.80: 20.20
Mn La
40 nm
(c)
Pt
Carbon
LSAT
0.2 µm
(d)
Ti
Mn4N
LSAT(001)
10 nm

Fig. 10